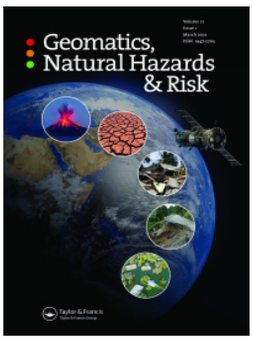

Geomatics, Natural Hazards and Risk

ISSN: (Print) (Online) Journal homepage: https://www.tandfonline.com/loi/tgnh20

AE energy evolution during CJB fracture affected by rock heterogeneity and column irregularity under lateral pressure

Bin Gong, Yongyi Wang, Tao Zhao, Chun'an Tang, Xiaoyu Yang & Tiantian Chen

To cite this article: Bin Gong, Yongyi Wang, Tao Zhao, Chun'an Tang, Xiaoyu Yang & Tiantian Chen (2022) AE energy evolution during CJB fracture affected by rock heterogeneity and column irregularity under lateral pressure, Geomatics, Natural Hazards and Risk, 13:1, 877-907, DOI: 10.1080/19475705.2022.2047114

To link to this article: https://doi.org/10.1080/19475705.2022.2047114

© 2022 The Author(s). Published by Informa UK Limited, trading as Taylor & Francis Group.

Published online: 10 Mar 2022.

Submit your article to this journal

Article views: 117

View related articles

View Crossmark data

Full Terms & Conditions of access and use can be found at
https://www.tandfonline.com/action/journalInformation?journalCode=tgnh20

GEOMATICS, NATURAL HAZARDS AND RISK
2022, VOL. 13, NO. 1, 877–907
https://doi.org/10.1080/19475705.2022.2047114

Taylor & Francis
Taylor & Francis Group

OPEN ACCESS Check for updates

AE energy evolution during CJB fracture affected by rock heterogeneity and column irregularity under lateral pressure

Bin Gong[a], Yongyi Wang[b], Tao Zhao[a], Chun'an Tang[b], Xiaoyu Yang[c] and Tiantian Chen[d]

[a]Department of Civil and Environmental Engineering, Brunel University London, London, UK; [b]State Key Laboratory of Coastal and Offshore Engineering, Dalian University of Technology, Dalian, China; [c]School of Civil Engineering, Chongqing Jiaotong University, Chongqing, China; [d]School of Resources and Civil Engineering, Northeastern University, Shenyang, China

ABSTRACT

Considering that the mechanical mechanism and energy release law of gradual failure of columnar jointed basalt (CJB) are affected by lateral pressure, rock heterogeneity and column irregularity, etc., the numerical CJB models with various column dip angles, irregularity degrees of column and lateral pressures were established through the digital image correlation. The progressive failure process and released energy of CJBs were simulated under the loading rate of 0.05 mm/step based the continuum mechanics and statistical damage theory. The influences of rock inhomogeneity, column irregularity degree, and model boundary on the nonlinear deformation and failure of CJB were comprehensively investigated. The results demonstrate that the effect of the inhomogeneity index depends on column dip angle, and the equivalent deformation modulus of CJBs is more sensitive to the inhomogeneity index than the lateral pressure. Moreover, the compressive strength along the direction perpendicular to the column axis basically decreases with column irregularity degree increasing when the meso strength of rock is 120 MPa. Besides, the mechanical properties and elastic energy of irregular CJBs are greatly affected by the model boundaries. These achievements will contribute to understanding the inner failure mechanism and energy evolution of CJBs.

ARTICLE HISTORY
Received 5 December 2021
Accepted 23 February 2022

KEYWORDS
Columnar jointed basalts; acoustic emission; rock heterogeneity; column irregularity; lateral pressure

1. Introduction

As a kind of columnar jointed rock mass (CJRM), columnar jointed basalt (CJB) is often considered relevant to basalt eruption and overflow. They can be observed in many places in the world including Europe, Asia, North America, etc. (Xiao et al.

CONTACT Yongyi Wang 07youki@mail.dlut.edu.cn State Key Laboratory of Coastal and Offshore Engineering, Dalian University of Technology, Dalian 116024, China

© 2022 The Author(s). Published by Informa UK Limited, trading as Taylor & Francis Group.
This is an Open Access article distributed under the terms of the Creative Commons Attribution License (http://creativecommons.org/licenses/by/4.0/), which permits unrestricted use, distribution, and reproduction in any medium, provided the original work is properly cited.

(a) (b)

Figure 1. Observed CJRMs or CJBs in the field: (a) CJRMs at Durham, UK; (b) CJRMs at Staffa, UK (Phillips et al. 2013).

2014; Ni et al. 2015; Weinberger and Burg 2019; Chao et al. 2020; Shi et al. 2020; Que et al. 2021). For example, the construction of large-scale hydropower stations has been carried out in the southwestern area of China in recent decades, where CJBs are encountered. Figure 1 shows the field photographs of CJRMs or CJBs (Phillips et al. 2013).

Some researchers (Zhu et al. 2009; Zheng et al. 2010; Yan et al. 2012; Ni et al. 2015; Cui et al. 2016; Yan et al. 2018) have studied the anisotropy and lateral pressure effect of CJRMs or CJBs. Clearly, Yan et al. (2012) investigated the size effect of CJRM under triaxial compression state in terms of macroscopic equivalent elastic modulus using the discrete element method. Yan et al. (2018) studied the anisotropic of CJRM under triaxial compression by the finite difference method. Cui et al. (2016) discussed the effect of joint surfaces on equivalent deformation modulus (EDM) of CJRM using the jointed network finite element method. However, the progressive fracture processes or acoustic emission (AE) energy evolutions of the specimens were not fully analysed. Ni et al. (2015) investigated the size influence of equivalent elastic modulus of CJRM by the discrete element method. Zhu et al. (2009) and Zheng et al. (2010) also analysed the anisotropic features and size influence of CJRM using the Voronoi algorithm and the three-dimensional (3D) discrete element method, respectively. However, there are certain limitations for the traditional numerical approaches when capturing the continuous fracture process of jointed rock mass (Haeri et al. 2018a, 2018b, 2018c, 2018d). They also have difficulties in fully considering inhomogeneity, discontinuity, nonlinearity, etc. (Feng et al. 2022; Wang et al. 2022). Besides, the meso-damage model has been proven appropriate for simulating the failure mechanism of jointed rock specimen at the meso level (Zhou et al. 2020; Xu et al. 2021; Yu et al. 2021; Yuan et al. 2021; Zhou et al. 2022).

In terms of laboratory physical experiments, it is difficult to produce CJB (or CJRM) specimens with relatively actual mechanical parameters of joints. Nevertheless, Que et al. (2021) carried out the uniaxial compression experiment using the artificial CJRM samples containing quadrangular, pentagonal and hexagonal prisms. Jin et al. (2018) also conducted physical and numerical tests to determine the anisotropic parameters of CJBs. Ji et al. (2017) made small-scale samples containing geological structures similar to the real CJRM. Furthermore, Chao et al. (2020) monitored the permeability and porosity of self-prepared artificial samples with various columnar dip angles under cyclic loading and unloading. Shi et al. (2020) presented a way to determine the strengths using true triaxial experiment according to the Mohr–Coulomb or Hoek–Brown criteria. Xia et al. (2020) proposed an effective approach for constructing irregular CJRM samples by the 3D printing technology. Liu et al. (2010) investigated the fracture mechanisms of CJRM affected by loading-unloading path and stress-strain relationship under true triaxial stress environment. However, the artificial structural surfaces of the test samples were relatively simple, and hardly reflected the actual mechanical properties. Although Xiao et al. (2014, 2015) measured the deformation moduli and compressive strengths of CJRM samples with various column dip angles. But, the effect of cement layer on the mechanical parameters of CJRMs is significantly different from natural columnar joints. Ke et al. (2019) analysed the effect of the dip angle of columns and transverse joints on the anisotropy and fracture mechanisms of CJRMs under uniaxial loading. Generally, the natural features of rock masses cannot be represented appropriately in the experimental studies, such as the rock inhomogeneity, column irregularity degree and discontinuities. Simultaneously, the mesoscopic failure process can hardly be provided and discussed deeply.

The mechanical behaviour of CJBs (or CJRMs) shows typical anisotropy, heterogeneity and column irregularity because of the existence of columnar joint surfaces. For engineering projects, the rock masses generally suffer lateral pressures. Therefore, to conduct the stability assessment of CJB, as well as put forward the corresponding treatment measures of engineering rock masses, it will be of great value to understand the fracture mechanism and energy evolution laws of CJBs with varying heterogeneity and column irregularity under lateral pressure. In this article, the digital images of CJB samples were transformed into the inhomogeneous models. Then, a group of numerical tests were carried out. The modelled results were compared with the related experiments to prove the validity and correctness. Then, the progressive fracture process and AE energy release of CJB along the direction perpendicular or parallel to the column axis were captured. Additionally, the influence of certain factors on the mechanical properties and AE energy of CJB were further discussed.

2. Methodology

2.1. The RFPA method improved by DIC

The rock failure process analysis (RFPA) method has been developed for modelling the gradual fracture process of rock mass (Tang and Kou 1998; Liang 2005; Li et al. 2011; Yu et al. 2015). The location where new cracks will initiate and the way how

they will develop are unnecessarily assumed beforehand. Meanwhile, the correctness and effectiveness of the RFPA method have been verified by many numerical benchmarks (Tang et al. 2001; Xu et al. 2013; Gong et al. 2022). Besides, it has been widely used in studying failure mode and stability of jointed rock masses (Li et al. 2009; Yang et al. 2015; Liu et al. 2017; Zhou et al. 2018).

The digital image correlation (DIC) technology was applied to enhance the model establishment ability of RFPA. Namely, the digital image consisting of many square pixels was used to establish the numerical model through the grey threshold segmentation. In the three-dimensional space, the pixels of the image can be transferred into finite elements by extending them to a specific thickness t along the normal direction. Then, the numerical model can be built up by determining the element coordinates according to the spatial position of every pixel. The grey value of one pixel was used to classify it into joint or rock materials and assign related material properties. After that, the obtained inhomogeneous model can be seen in Figure 2(a).

Besides, the constitutive curve of an element under uniaxial stress state is depicted in Figure 2(b). According to Mazars and Pijaudier-Cabot (1989), the constitutive curve under complicated stress states can be therefore gained by extending the constitutive curve under uniaxial state.

2.2. Strength criterion and mechanical damage

For the RFPA method, the stress/strain relationship of an element shown in the third quadrant in Figure 2(b) will be applied under uniaxial tension. The related tensile strength criterion can be expressed as follows:

$$\sigma_3 \leq f_t \tag{1}$$

where f_t is the uniaxial tensile strength.

Meanwhile, the Mohr-Coulomb criterion is applied as the compression-shear strength criterion shown as follows:

$$\sigma_1 - \frac{1+\sin\varphi}{1-\sin\varphi}\sigma_3 - f_c \geq 0 \tag{2}$$

where σ_1 and σ_3 are the maximum principal stress and the minimum principal stress, respectively. φ and f_c are the internal friction angle and the uniaxial compressive strength, respectively.

For the elastic damage approach, if the stress state researches the strength criterion, the elastic modulus of the element would be reduced continuously with the load increasing. The degraded elastic modulus is described as follows:

$$E = (1 - D)E_0 \tag{3}$$

where D is termed the damage variable; E is the degraded elastic modulus of a failure element; E_0 is the original elastic modulus of an element before failure.

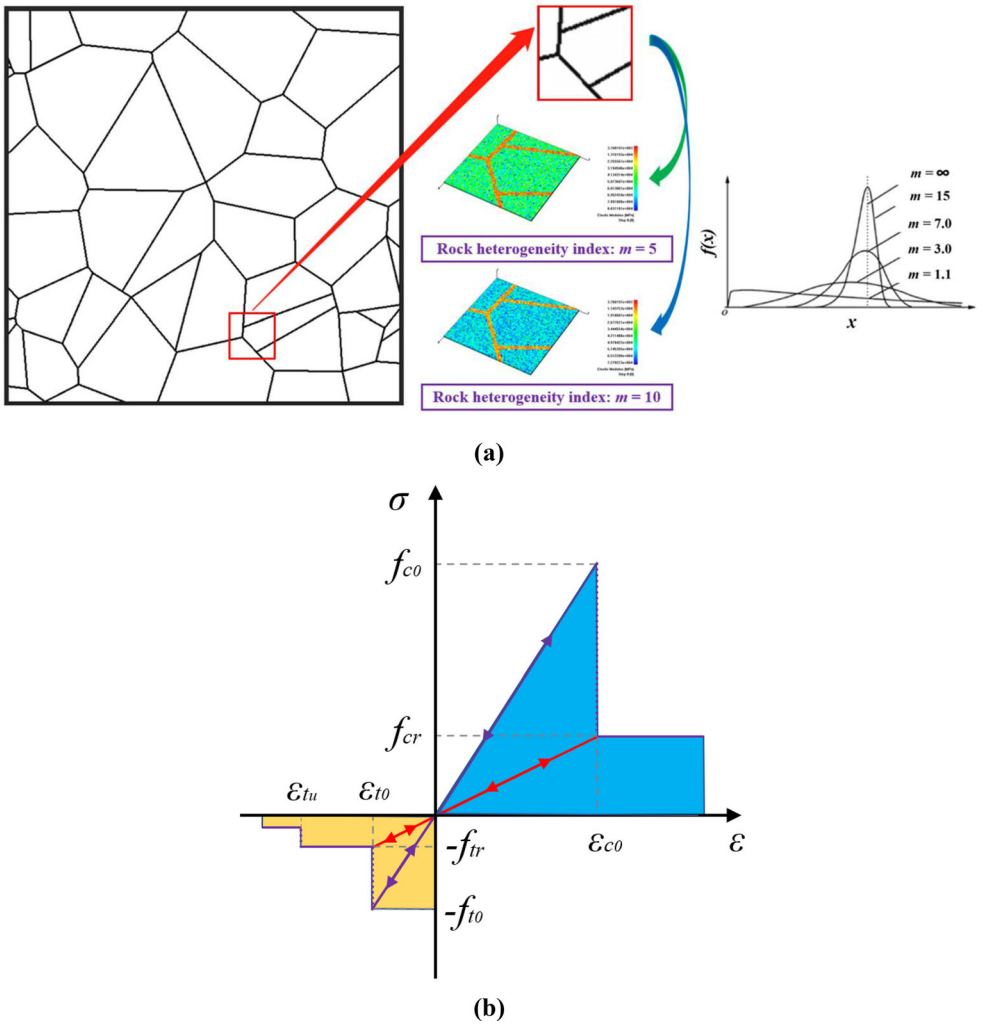

Figure 2. (a) Digital image and inhomogeneous numerical model after transformation; (b) the constitutive relation of an element under uniaxial stress state.

When the tensile strength criterion is researched, the damage variable D will be described using the Eq. (4) (Tang et al. 2015):

$$D = \begin{cases} 0 & \varepsilon > \varepsilon_{t0} \\ 1-\lambda\varepsilon_{t0}/\varepsilon & \varepsilon_{tu} < \varepsilon \leq \varepsilon_{t0} \\ 1 & \varepsilon \leq \varepsilon_{tu} \end{cases} \tag{4}$$

where λ is termed the residual strength coefficient defined as $\lambda = f_{tr}/f_t$; f_t and f_{tr} are the uniaxial tensile strength and the residual tensile strength, respectively; ε_{t0} is the elastic limit strain under tension defined by $\varepsilon_{t0} = f_t/E_0$; ε_{tu} is the ultimate strain indicating that the element is fully damaged, and it can be determined by $\varepsilon_{tu} = \eta\varepsilon_{t0}$, where η represents the coefficient of ultimate strain.

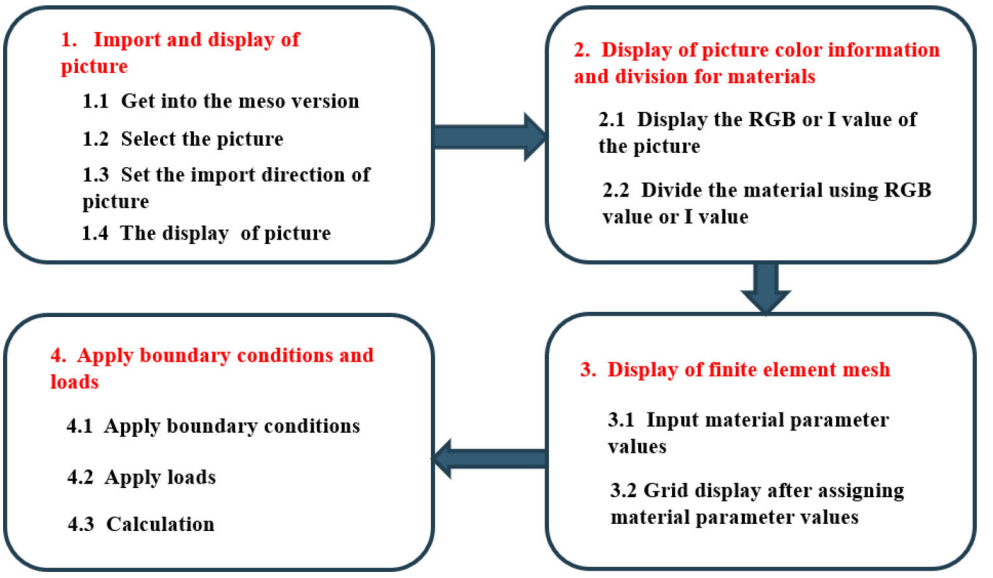

Figure 3. Picture import process of the DIC-enhanced RFPA method.

Furthermore, if a meso element fails under the compression shear state, the damage variable $\boldsymbol{D}$ will be determined using the Eq. (5) (Tang et al. 2015):

$$\boldsymbol{D} = \begin{cases} 0 & \varepsilon < \varepsilon_{c0} \\ 1-\lambda\varepsilon_{t0}/\varepsilon & \varepsilon \geq \varepsilon_{c0} \end{cases} \tag{5}$$

where λ is the residual strength coefficient defined as $\lambda = f_{cr}/f_c$; f_c and f_{cr} are the uniaxial compressive strength and the residual compressive strength, respectively; ε_{c0} is the elastic limit strain under compression defined by $\varepsilon_{c0} = f_c/E_0$. In the RFPA method, the AE event and related energy can be recorded. The picture import process of the DIC-enhanced RFPA method is given in Figure 3.

2.3. Benchmark

The physical tests were used to prove the effectiveness of the numerical method. Ji et al. (2017) produced the CJRM samples by bonding the regular hexagonal prisms made of cement, fine sand, water and water reducer using a mass mixing ratio of 1:0.5:0.35:0.002. Then, the samples were compressed along the axis. Simultaneously, Xiao et al. (2014) conducted a group of uniaxial compression experiments using CJRM samples made of gypsum, cement and water with a mass mixing ratio of 3:1:3.2.

The related numerical models with 50 mm in width and 100 mm in height were established and tested under plane strain, and the diameter of the hexagonal prisms in the models was 10 mm. They were compressed along the direction I (II) perpendicular to the column axis as well as the direction parallel to the column axis (β from 0° to 90° with the interval of 15°). A group of digital images were transferred into the numerical samples, as displayed in Table 1. The material properties were

Table 1. Schematic diagram of joint setting, geometry and load of the transformed finite element models for numerical verification.

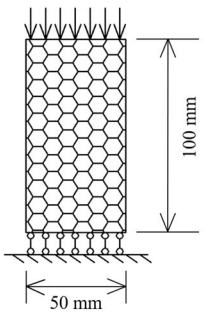 The direction I perpendicular to column axis	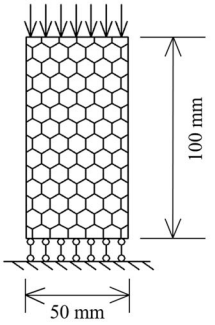 The direction II perpendicular to column axis	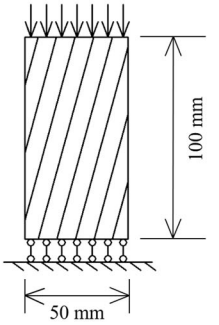 The direction parallel to column axis (β=15°)
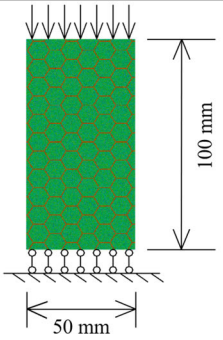 The direction I perpendicular to column axis	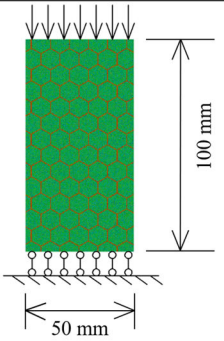 The direction II perpendicular to column axis	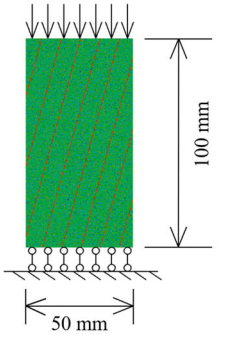 The direction parallel to column axis (β=15°)

Table 2. Mechanical parameters of finite element models for numerical validation.

Material type	Heterogeneity index	Elastic modulus (GPa)	Uniaxial compressive strength (MPa)	Poisson's ratio	Friction angle (°)	Residual strength coefficient
Basalt	5	60	120	0.2	56.15	0.1
Joint	5	15	30	0.25	36	1

presented in Table 2, which was referred to the related literature of CJB (Liu et al. 2010; Zheng et al. 2010; Yan et al. 2012; Ni et al. 2015; Ji et al. 2017; Ke et al. 2019; Que et al. 2021). The displacement-controlled loading way was applied with a rate of 0.005 mm/step until macroscopic instability.

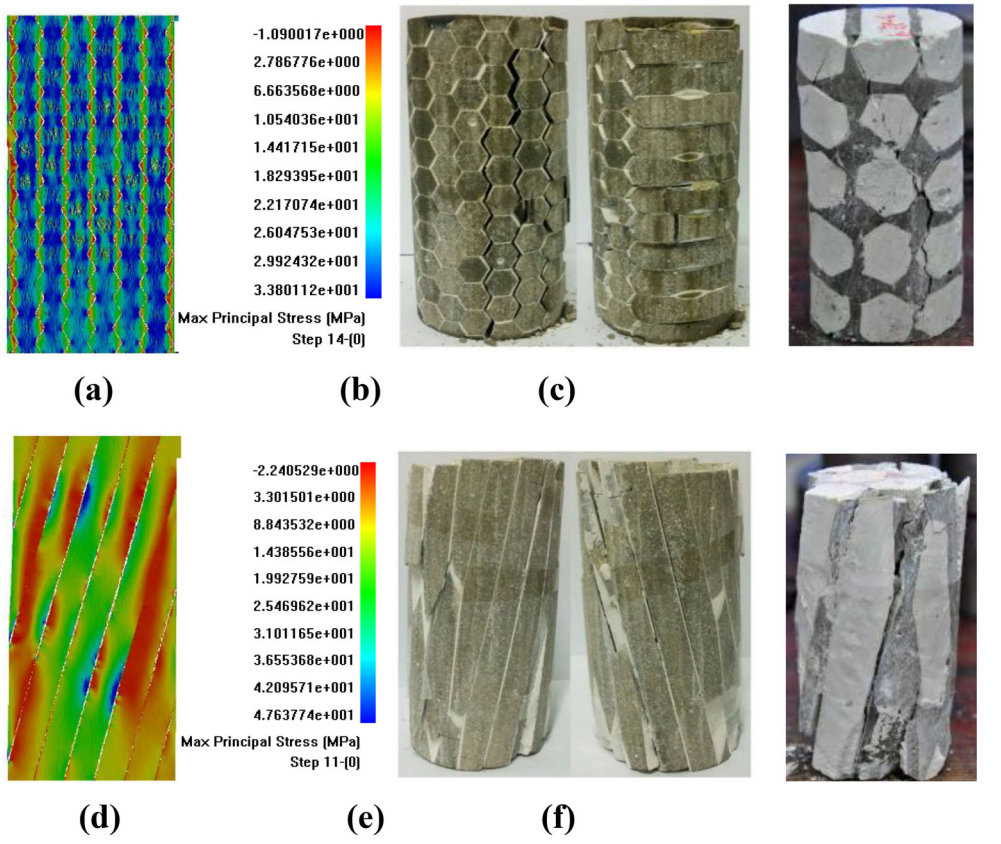

Figure 4. Comparison of failure modes between physical experiments and numerical tests: (a) the direction I perpendicular to column axis in numerical test; (b) physical experiment (Ji et al. 2017); (c) physical experiment (Xiao et al. 2014); (d) $\beta = 15°$, the direction parallel to column axis in numerical test; (e) physical experiment (Ji et al. 2017); (f) physical experiment (Xiao et al. 2014).

The normalized uniaxial compression strength coefficient between physical experiments and simulated results were comprised as shown in Figure 4. We can see that the main features of the simulated failure patterns almost coincide with the physical experiments. Therefore, the DIC-enhanced RFPA provides a reliable approach to study the mechanical behaviours of CJRM.

2.4. Numerical configuration

For the numerical models, the column length and diameter were 0.5–3 m and 13–25 cm, respectively. The parameter values and calculation condition settings are listed in Table 3. The influencing factors include lateral pressures, column dip angles, rock inhomogeneity indexes, the irregularity degrees of columns, boundary conditions, etc.

In the numerical tests of CJBs under lateral pressure, the size of each element keeps same. Therefore, the element number varies, and for instance, it is 608,400 for

Table 3. Parameters and calculation conditions of CJB models under lateral pressure.

	Parameter values and calculation condition settings
Lateral pressures (MPa)	0, 2, 4, 6, 8
Model size (m)	3×3
Column dip angles β of model along the direction parallel to column axis (°)	0, 15, 30, 45, 60, 75, 90
Rock heterogeneity indexes	5, 10
The irregularity degrees of columns	Completely regular columns, approximately regular columns, moderately regular columns, irregular columns
Model boundaries	The case between plane stress and plane strain, the case of plane strain

the 3-m sample. Meanwhile, according to Cui et al. (2016), four different columns are used, i.e. completely regular column, approximately regular column, moderately regular column and irregular column. Figure 5(a)–(j) show the diagram of typical setup and boundary condition for the CJBs with the varying irregularity degree of column. Furthermore, two kinds of boundary conditions are considered, i.e. the case of plane strain and the case between plane stress and plane strain. For plane strain, the displacement constraints are set on both sides along the normal direction of the model plane. It corresponds to the situation that the deformation of rock masses is fixed along one direction, like the surrounding rocks of a tunnel along its axis, as depicted in Figure 5(e,i). In the case between plane stress and plane strain, the displacement constraints are set on one side along the normal direction of the model plane. It represents the rock mass with a fixed direction and a free surface, such as tunnel wall along the direction towards free surface, as presented in Figure 5(f,g,j). The displacement-controlled load way was applied on the top surface of the model with the loading rate of 0.05 mm/step.

In nature, the mechanical properties of joint are generally weaker than intact rocks (Gui and Zhao 2015). Meanwhile, rhe selection of joint parameter could affect the deformation and strength of jointed rock masses (Sun et al. 2012). But, the ratio of parameter values between joints and intact rocks is not completely clear. According to the above benchmarks and corresponding researches of CJBs (Liu et al. 2010; Zheng et al. 2010; Yan et al. 2012; Ni et al. 2015; Ji et al. 2017; Ke et al. 2019; Que et al. 2021), the parameter values of joints and rocks are shown in Table 4.

3. Result and analysis

3.1. Progressive failure process and AE energy evolution characteristics of completely regular CJBs with lateral pressure along the direction I perpendicular to column axis

Figure 6 displays the stress-strain relationship of 3-m sample with lateral pressure of 6 MPa along the direction I perpendicular to the column axis, as well as the minor principal stress diagrams describing the crack initiation and growth, where the red areas represent the existence of the high stress concentrations.

As presented in Figure 6(a–f), the high stress concentrations occur in the vertical joints of the sample in the beginning. But, they are not obvious. Then, the stress concentrations of vertical joints disappear. However, the top of the sample doesn't

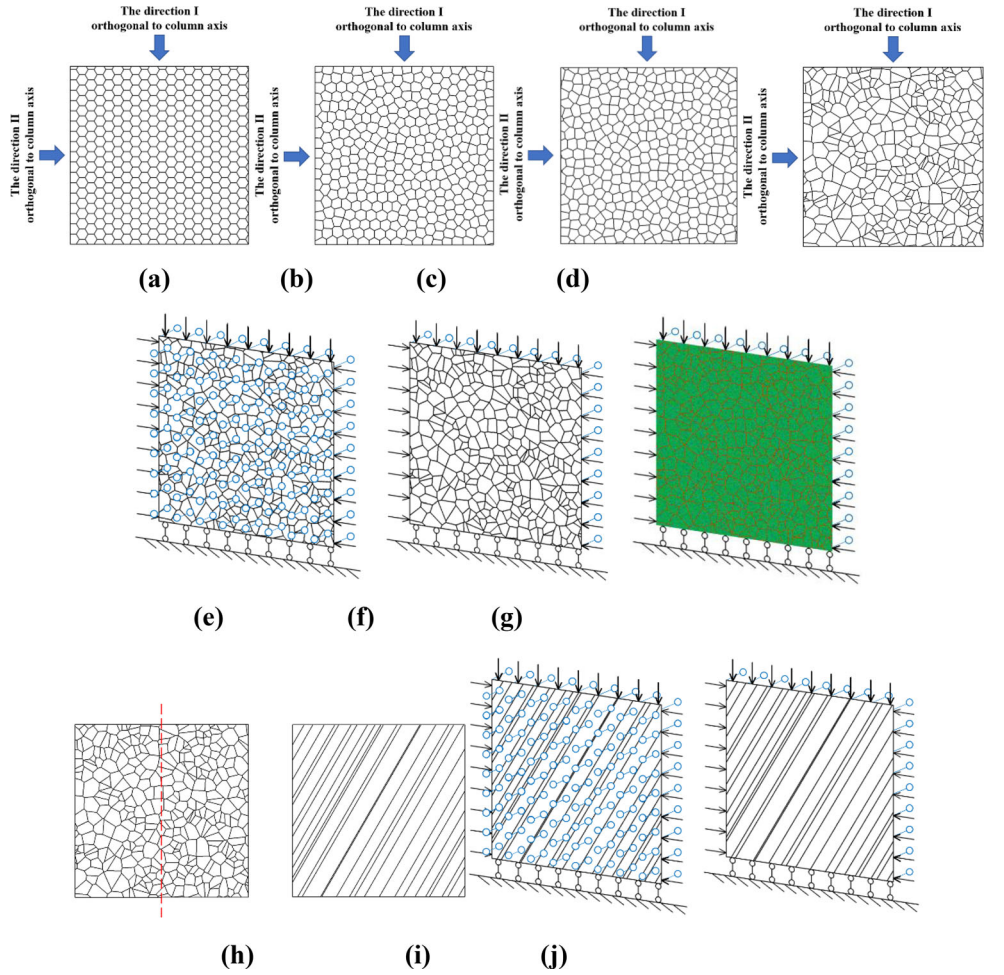

Figure 5. Model setup and boundary condition for the CJBs with different irregularity degrees of columns: (a) completely regular columns; (b) approximately regular columns; (c) moderately regular columns; (d) irregular columns; (e) the irregular CJBs in the case of plane strain; (f) the irregular CJBs in the case between plane stress and plane strain; (g) the inhomogeneous model after digital image transformation; (h) the model slices along the direction perpendicular and parallel to column axis; (i) the irregular CJBs along the direction parallel to column axis in the case of plane strain; (j) in the case between plane stress and plane strain.

Table 4. Mechanical parameters of rock and joint of CJBs.

Material type	Heterogeneity index	Elastic modulus (GPa)	Uniaxial compressive strength (MPa)	Poisson's ratio	Friction angle (°)	Residual strength coefficient
Basalt	5, 10	60	120	0.2	56.15	0.1
Joint	5	15	30	0.25	36	1

damage obviously. After that, the high stress concentrate at the individual columns in the top-left and top-right areas of the sample. When the stress value reaches its peak of the stress-strain relationship, the stress concentrations of columns in the top-left

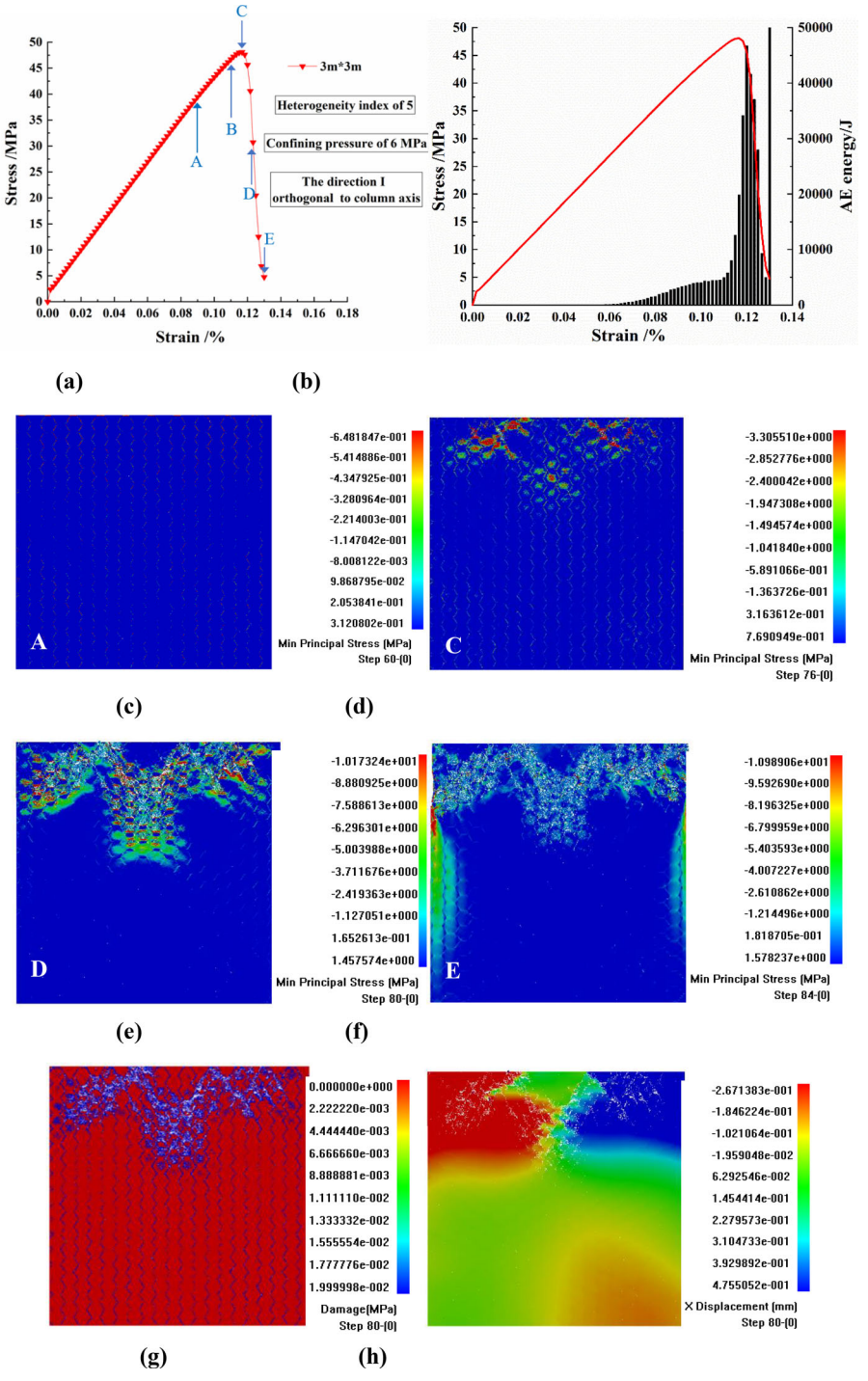

Figure 6. Gradual fracture process and failure mode of the completely regular CJBs along the direction I perpendicular to column axis: (a,b) the stress–strain curve and AE rate; (c–f) the minimum principal stress diagrams at Points A, C, D, and E; (g) the damage diagram; (h) the displacement diagram along the *x* axis; (i) the displacement diagram along the *z* axis; (j) the AE diagram (the 3-m specimen with column diameter of 20 cm, heterogeneity index of 5, lateral pressure of 6 MPa).

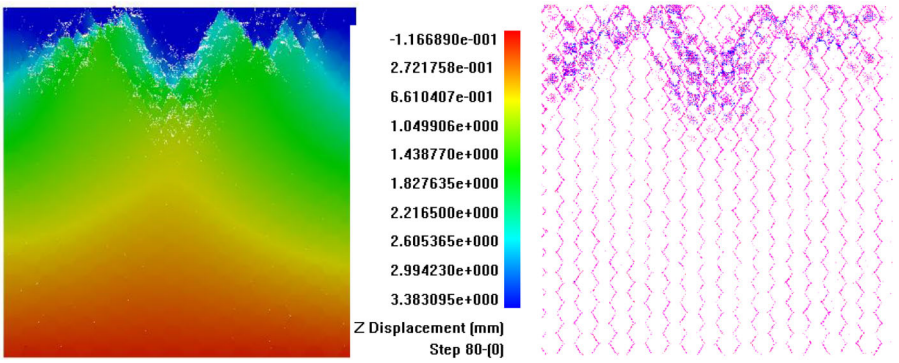

Figure 6. Continued.

and top-right areas of the sample develop further, leading to new cracks. Meanwhile, the stress concentrations appear at the columns in the upper-middle of the sample. Then, the load grows continuously while the stress drops to Point D. It can be seen that in the upper-left, upper-middle and upper-right areas of the sample, the fractures of columns are obvious. Finally, with the stress dropping to Point E, the columns in the upper area of the specimen get broken more severely. Under the role of lateral pressure, the specimen is squeezed and deformed to a certain extent. In Figure 6(b), the AE energy of the specimen shows single peak distribution. Simultaneously, it is the fractures of columns at the upper area of the sample that result in the peak value of AE energy. Then, a sudden increase occurs at the end of AE energy, which is caused by the failure of the whole specimen during the loading process of numerical test. One of the advantages of the DIC-enhanced RFPA in numerical test is also shown. Namely, the whole process of AE energy evolution from initial loading to instability under lateral pressure can be revealed.

As we can be seen from Figure 6(g), there is an M-shaped damage area at the upper part of the sample, while in other areas of the specimen, the vertical joints are damaged. The x-direction displacement diagram in Figure 6(h) shows that the x-direction extrusion of the upper area of the sample is distinct, which is mainly because of the damage, fracture of elements and then the extrusion deformation of the upper part of the specimen. As depicted in the z-direction displacement diagram in Figure 6(i), the sedimentation mainly occurs near the top area of the sample, and the main sedimentation part is distributed in a fluctuating strip way. The AE diagram in Figure 6(j) shows that the vertical joints of the specimen are subjected to compression and shear, which is displayed by pink AE, while the columns at the upper area of the sample are with both compressive failure AE and tensile failure AE (blue AE).

3.2. Progressive failure process and AE energy evolution characteristics of irregular CJBs with lateral pressure along the direction I perpendicular to column axis

Figure 7 indicates the stress–strain relationship of the 3-m irregular CJB sample with lateral pressure of 6 MPa along the direction I perpendicular to the column axis, as

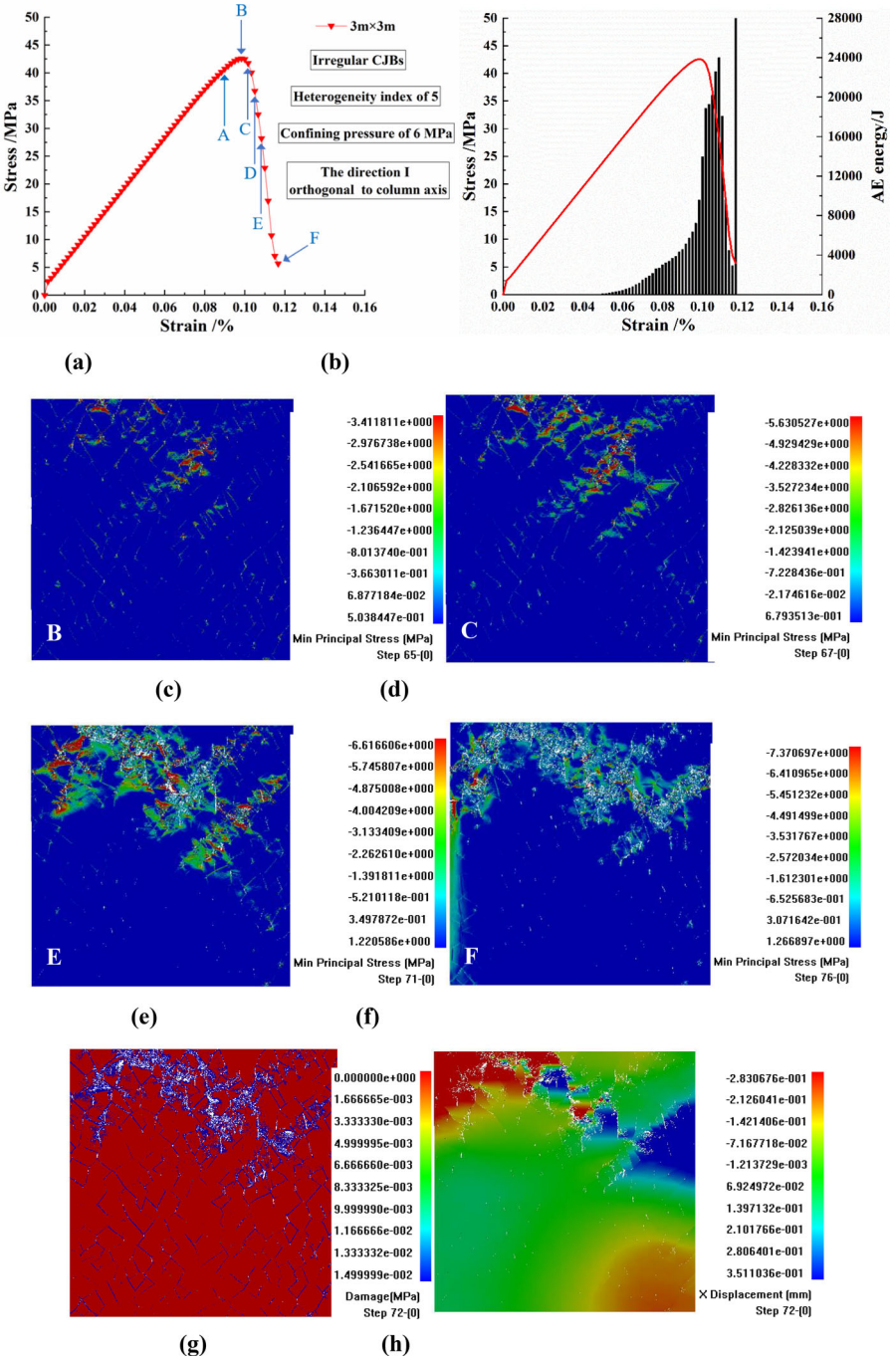

Figure 7. Gradual fracture process and failure mode of the irregular CJBs along the direction I: (a,b) the stress–strain curve and AE rate; (c–f) the minimum principal stress diagrams at Points B, C, E and F; (g) the damage diagram; (h) the displacement diagram along the *x* direction; (i) the displacement diagram along the *z* direction; (j) the AE diagram (the 3-m specimen with column diameter of 20 cm, heterogeneity index of 5, lateral pressure of 6 MPa).

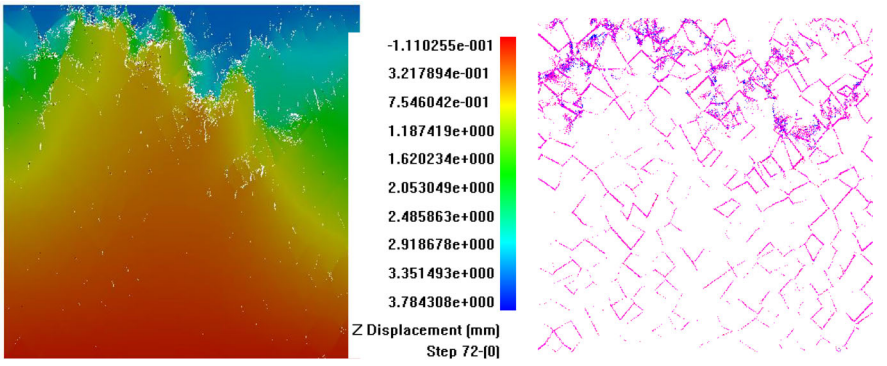

Figure 7. Continued.

well as the minor principal stress diagrams. According to Figure 7(a–f), at Point A, the weak compression-shear slip occurs at sporadic location of joints in the whole sample. Meanwhile, there are high stress concentrations at a few local areas of the sample. When the load is carried out to the peak Point B, the compression shear slip of joints within the upper area of the specimen further develops, and the stress concentration at several columns is relatively clear. With the stress dropping to Point C, some cracks initiates and propagates at a few columns at the upper-middle of the sample. When the stress decreases to Point D, these cracks continue to develop and the stresses at the crack tips are concentrated. At Point E, more columns get broken in the upper are of the sample. Finally, the breakage of the columns in the upper area of the sample intensifies at Point F. Figure 7(b) shows the whole process of AE energy evolution of the CJBs specimen from loading to overall instability failure. In Figure 7(b), the AE energy of the specimen is distributed with one single peak. Simultaneously, the maximum value of the AE energy is mainly produced by the fractures of columns at the upper area of the sample.

As presented in Figure 7(g), the columns within the upper area of the sample are seriously damaged. The vertical joints and oblique joints in other areas of the specimen are damaged as well. The x-direction displacement diagram in Figure 7(h) shows that the x-direction extrusion is obvious in the top-left side and the middle-right side of the sample, which is mainly because of the asymmetric cracks and damage in the irregular CJB specimen. Furthermore, the z-direction displacement diagram in Figure 7(i), the sedimentation occurs near the top of the sample, while the sedimentation is transmitted to a deeper depth in the right side of the sample. The AE diagram in Figure 7(j) shows that the columns in the upper area of the sample are with both compressive failure AE (pink AE) and tensile failure AE (blue AE), while the vertical and oblique joints of the specimen are with pink AE due to compression and shear.

3.3. Progressive failure process and AE energy evolution characteristics of irregular CJBs with lateral pressure along the direction parallel to column axis

Figure 8 indicates the stress–strain relationship of the 3-m irregular CJBs sample with lateral pressure of 6 MPa and $\beta = 30°$, as well as the minor principal stress diagrams

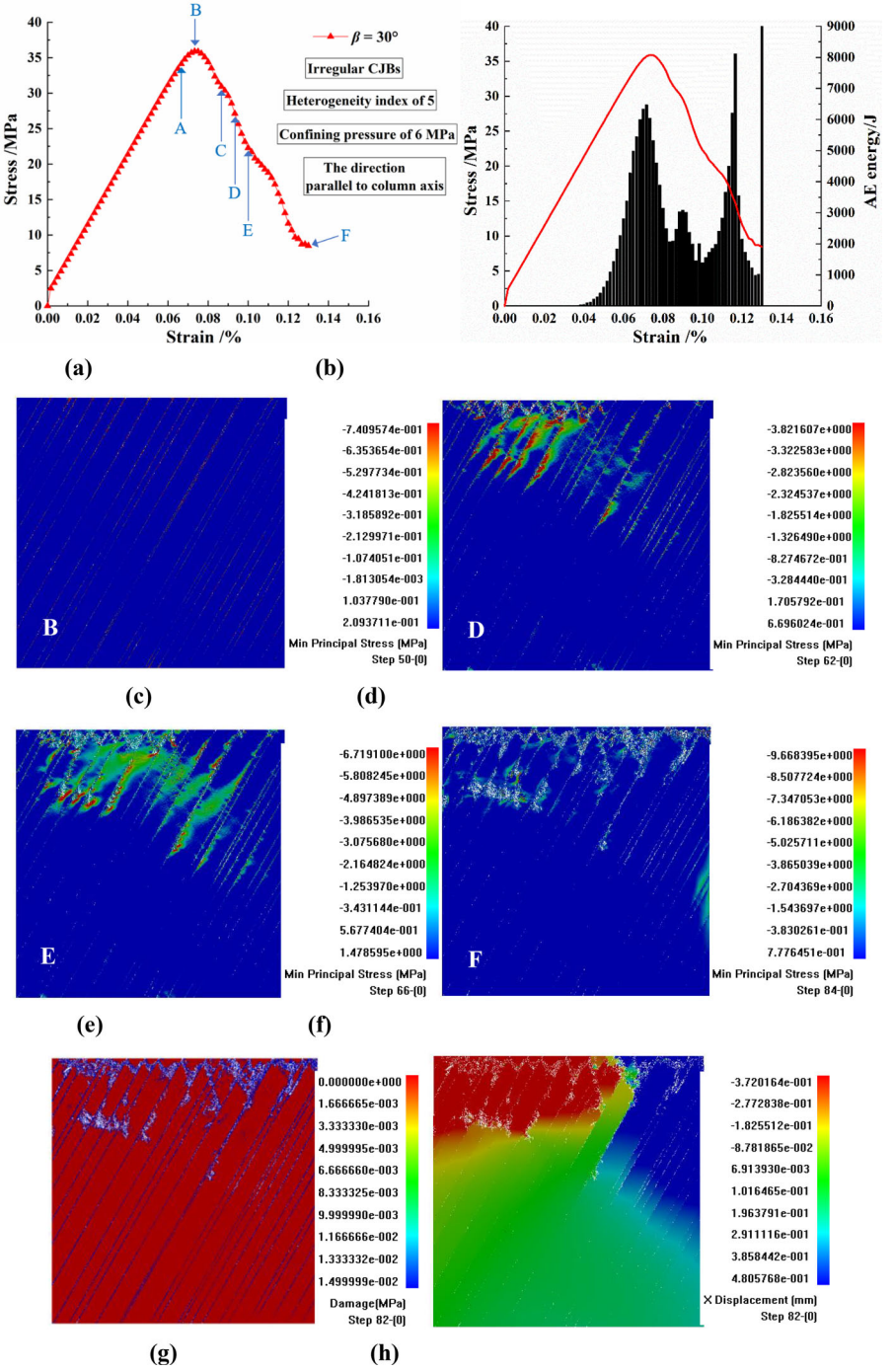

Figure 8. Gradual fracture process and failure mode of the irregular CJBs with $\beta = 30^{\circ}$ along the direction parallel to column axis: (a, b) the stress–strain curve and AE rate; (c–f) the minimum principal stress diagrams at Points B, D, E and F; (g) the damage diagram; (h) the displacement diagram along the *x* direction; (i) the displacement diagram along the *z* direction; (j) the AE diagram (the 3-m specimen with column diameter of 20 cm, heterogeneity index of 5, lateral pressure of 6 MPa).

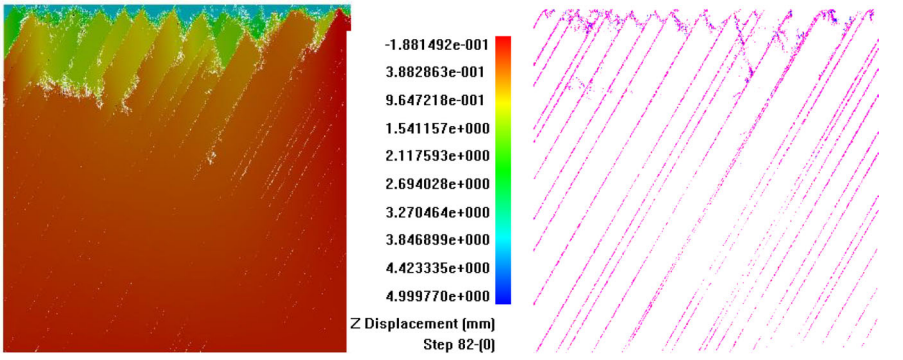

(i) (j)

Figure 8. Continued.

describing the failure process of rock sample, where the red areas reflect the high stress concentrations.

According to Figure 8(a–f), at Point A in the loading stage, the columnar joints inside the sample have high stress concentrations. When the load reaches the peak Point B, there is a tendency of compression-shear damage slip at some local locations of the joints. With the stress dropping to Point C, the compression-shear slip appears at the joints in the upper area of the sample. At the top of the sample, the stress concentration is obvious and the crack initiation occurs. When the stress drops to Point D, new cracks further initiate and develop at the top of the specimen, and the stresses are concentrated at the edges of some columns in the upper area of the sample. With the stress further dropping to Point E, the cracks initiate and propagate at the edges of several columns and at the original stress concentration areas. Furthermore, high stress concentrations occur at the crack tips. Finally, when the stress decreases to Point F, the breakage of the columns intensifies at the upper area of the sample. In Figure 8(b), the AE energy of the specimen is distributed in a double-peaks way. Clearly, the first AE energy peak is induced by the compression-shear slip and damage of the columnar joints, and the second AE energy peak is because of the fractures of the columns within the upper area of the sample. In the last stage of AE energy, there is also a sudden increase of AE energy, indicating that the specimen is with overall instability failure.

As depicted in Figure 8(g), the damage development of the columns in the upper area of the sample are distinct, while in the other areas of the specimen, damage is mainly distributed in the columnar joints. The x-direction displacement diagram in Figure 8(h) shows that there is asymmetric extrusion deformation in the upper-left and upper-right areas of the sample, which is mainly affected by the inclination of the columns. Meanwhile, the z-direction displacement diagram in Figure 8(i), the sedimentation mainly occurs near the top of the specimen. The AE diagram in Figure 8(j) shows that the pink AE appears at the columnar joints under compression and shear, and there are both compressive failure AE and a few tensile failure AE (blue AE) at the columns near the top of the specimen.

3.4. Effect of rock inhomogeneity index on mechanical properties and AE energy of CJBs under lateral pressure

As presented in Figure 9(a,b), in terms of compressive strength (CS), for the cases of the directions I/II perpendicular to the column axis, when the inhomogeneity index is 5 and 10, the CS of sample grows up gradually with the lateral pressure increasing. In terms of EDM, for the cases of the directions I/II perpendicular to the column axis, when the inhomogeneity index is 5 or 10, the EDM of specimen increases at first and then grows slowly with the lateral pressure increasing. In addition, when the lateral pressure is large (for example, the lateral pressure of 8 MPa) and inhomogeneity index is 5 or 10, the EDM of sample along the direction II perpendicular to the column axis is larger than the direction I.

As shown in Figure 9(c–f), for the cases of the direction parallel to the column axis, when the inhomogeneity index is 5 or 10 and the lateral pressure is 2, 4, 6 or 8 MPa, the trend of the sample CS is U-shaped with the dip angle of columns increasing. When dip angle $\beta = 15°$–$60°$, the influence of the inhomogeneity index on the CS of specimen is very small. When dip angle $\beta = 0°$, $75°$ and $90°$, the influence of inhomogeneity index on that is obvious. Clearly, at $\beta = 0°$, $75°$ and $90°$, with the growth of rock inhomogeneity index (i.e. the less rock inhomogeneity), the CS of specimen increases. In terms of EDM, when the inhomogeneity index is 5 or 10 and the lateral pressure is 2, 4, 6 or 8 MPa, the EDM of specimen decreases in the beginning, then arises and then drops again with the dip angle increasing. Compared with the two factors of rock inhomogeneity index and lateral pressure, EDM is more sensitive to the inhomogeneity index and less sensitive to lateral pressure.

In Figure 9(g), the Points A–D correspond to the accumulated AE energy for the stress peaks, respectively. According to Figure 9(g), under the lateral pressure of 6 MPa, along the direction I (II), from the perspective of the sequence of the occurrence on the strain axis, the inhomogeneity indexes for accumulated AE energy corresponding to the strength peak of specimens are 5, 10, respectively; in the aspect of AE energy accumulation magnitude from little to large, the inhomogeneity indexes for that are 5, 10, respectively. It can be concluded that along the direction perpendicular to the column axis, when the rock is less inhomogeneity, the accumulated AE energy corresponding to the stress peak lags in the loading stage, and the corresponding quantity value increases.

It can be seen from Figure 9(h) that under the lateral pressures of 2 and 6 MPa, for the direction parallel to the column axis, from the perspective of the sequence of the occurrence on the strain axis, the inhomogeneity indexes for accumulated AE energy corresponding to the strength peaks of specimens are 10 and 5, respectively; that is, for the direction parallel to the column axis and $\beta = 30°$, the less rock inhomogeneity, the more forward the accumulated AE energy corresponding to the stress peak on the strain axis. In the aspect of AE energy accumulation magnitude from little to large, the inhomogeneity indexes for that are 5 and 10, respectively, but the difference is small.

3.5. Effect of irregularity degree of column on mechanical properties and AE energy of CJBs under lateral pressure

It can be seen from Figure 10(a–d) that along the direction I perpendicular to the column axis, when the lateral pressure of 6 MPa, with the column irregularity degree

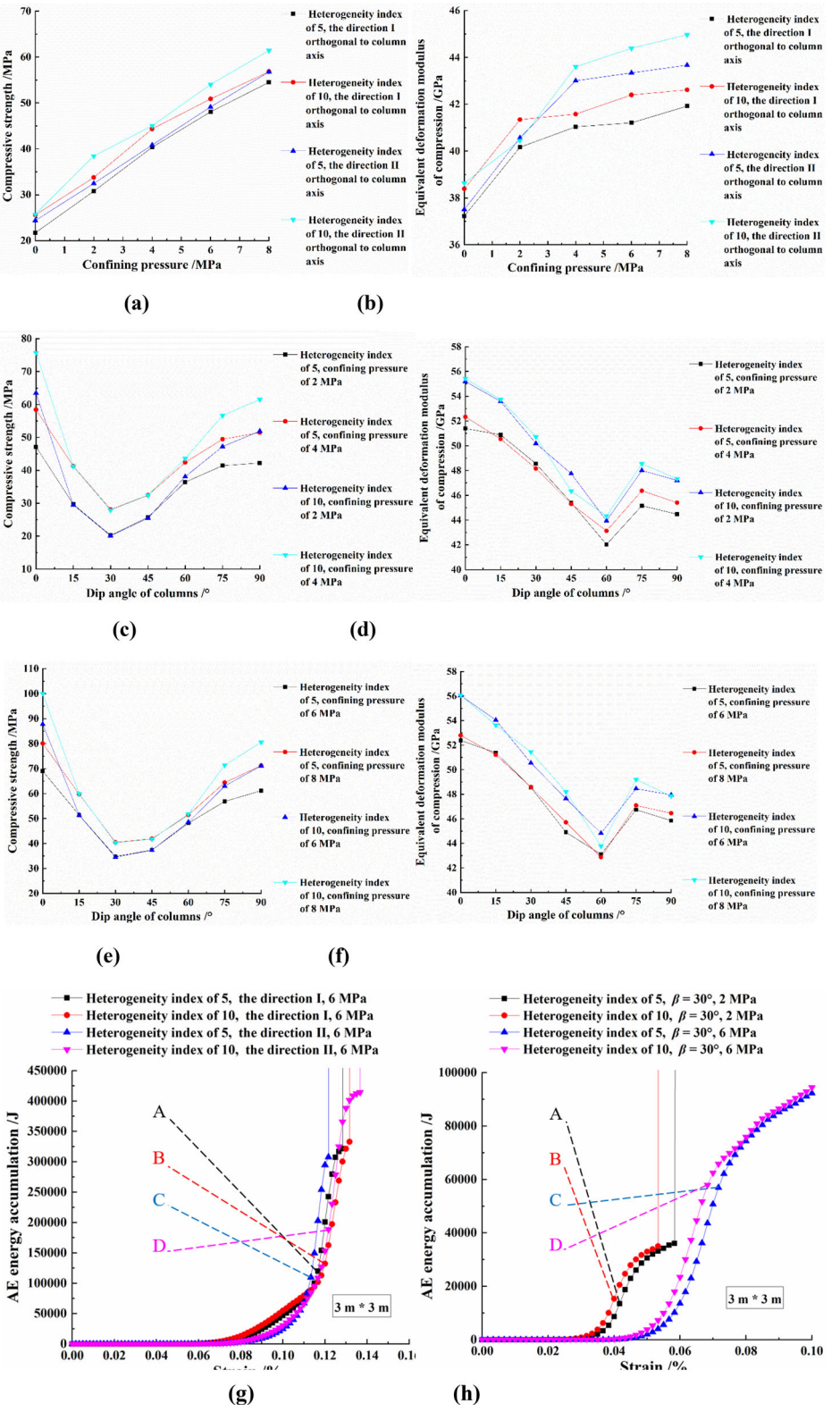

Figure 9. (a,c,e) The compressive strengths of samples with different heterogeneity indexes; (b,d,f) the equivalent deformation moduli; (g,h) the accumulated AE energy curves (the specimens with column diameter of 20 cm) (the Points A–D correspond to the AE energy accumulations for the peak stresses, respectively).

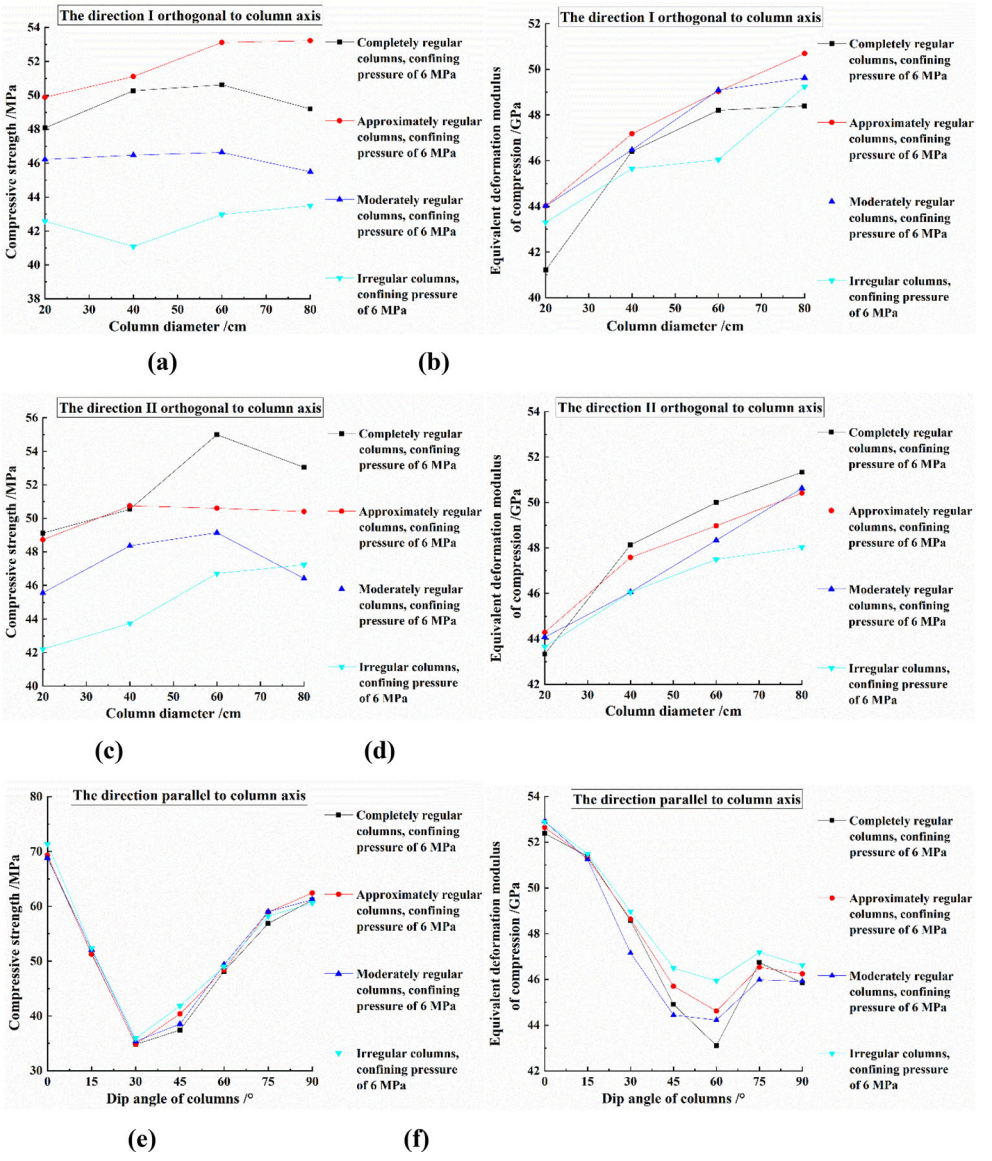

Figure 10. (a,c,e) The compressive strengths of samples along the direction I, II and the direction parallel to column axis; (b,d,f) the equivalent deformation moduli of samples along the direction I, II and the direction parallel to column axis; (g–i) the accumulated AE energy curves along the direction I, II and the direction parallel to column axis (the specimens with heterogeneity index of 5) (the Points A–D correspond to the AE energy accumulations for the peak stresses, respectively).

increasing, the CS of specimen increases and then decreases. For the case of the direction II perpendicular to the column axis and the lateral pressure of 6 MPa, with the irregularity degree of columns growing, the CS of the specimen reduces.

Along the directions I/II perpendicular to the column axis, EDM grows with the column diameter increasing. When the column diameter is 80 cm, EDM of completely regular columns is the smallest for the direction I perpendicular to the column axis, while that of irregular columns is the smallest along the direction II.

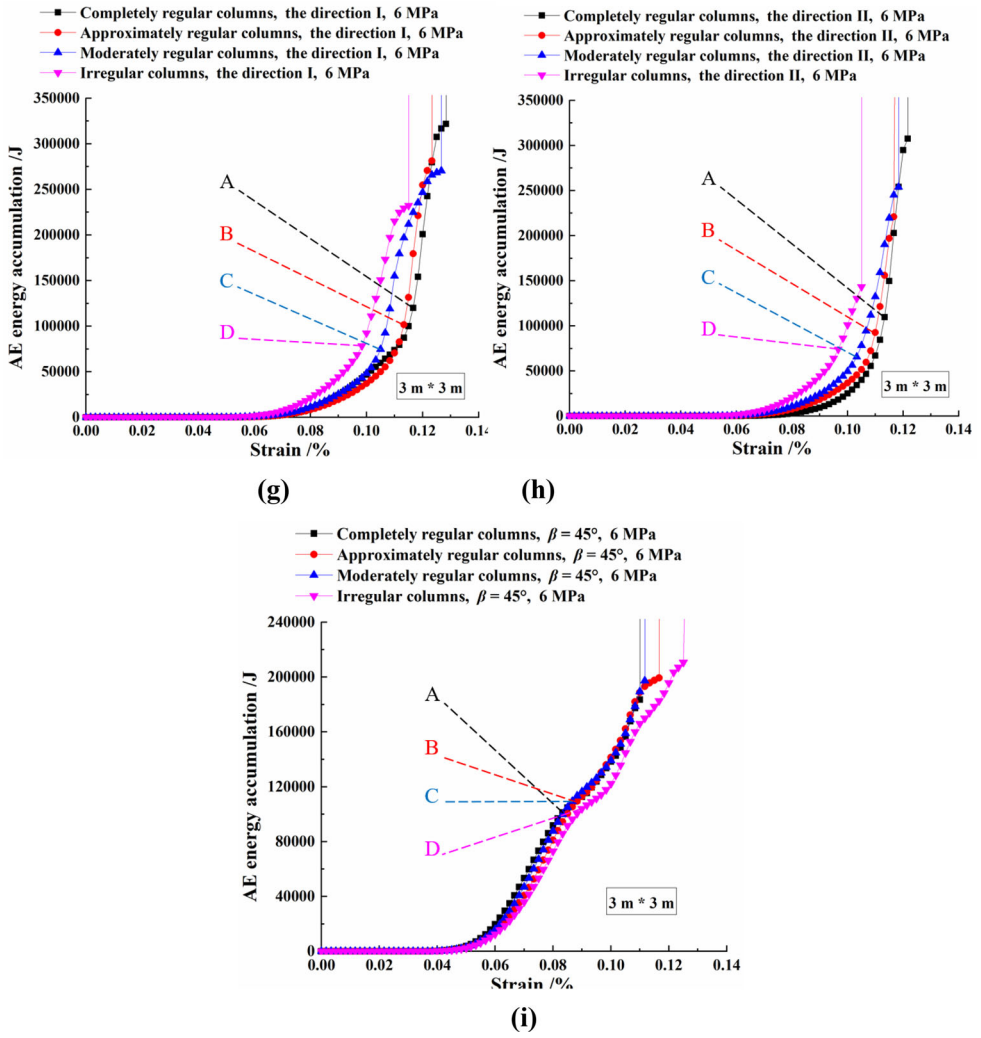

Figure 10. Continued.

As shown in Figure 10(e–f), for the case of the direction parallel to the column axis, when the lateral pressure is 6 MPa, the CS of the specimen with various irregularity degrees of columns indicates a V-shaped trend with the dip angle of columns increasing. When the dip angle of columns is $\beta = 45°$, the CSs of samples with various irregularity degrees of columns are different obviously. In the aspect of EDM, when the lateral pressure is 6 MPa, the EDMs of samples with various irregularity degrees of columns decrease at first, then increase, and then reduce or change slowly with the growth of the column dip angle.

According to Figure 10(g,h), under the lateral pressure of 6 MPa, along the direction I (II) perpendicular to the column axis, in terms of the sequence of the occurrence on the strain axis, the irregularity degrees of columns for accumulated AE energy corresponding to the strength peaks of specimens are irregular columns, moderately regular columns, approximately regular columns, completely regular

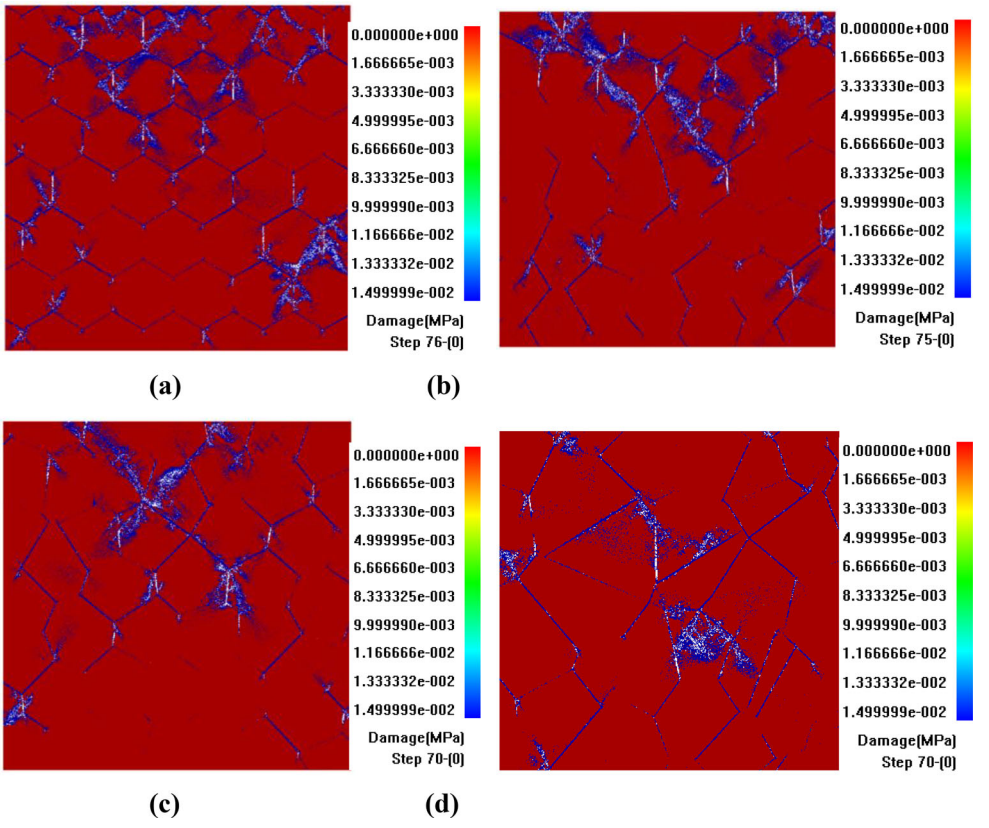

Figure 11. Failure modes of samples with various irregularity degrees of columns along the direction II perpendicular to column axis: (a) the completely regular CJBs; (b) the approximately regular CJBs; (c) the moderately regular CJBs; (d) the irregular CJBs (the 3-m specimens with column diameter of 60 cm, heterogeneity index 5, lateral pressure of 6 MPa).

columns, respectively; in terms of AE energy accumulation magnitude from little to large, the irregularity degrees of columns for that are irregular columns (moderately regular columns), approximately regular columns, completely regular columns, respectively.

As depicted in Figure 10(i), when the lateral pressure is 6 MPa, for the direction parallel to the column axis and $\beta = 45^{\circ}$, in terms of the occurrence sequence on the strain axis, the irregularity degrees of columns for accumulated AE energy corresponding to the strength peaks of specimens are completely regular columns, moderately regular columns, approximately regular columns, irregular columns, respectively; in terms of AE energy accumulation magnitude from little to large, the irregularity degree of column for that are completely regular columns, irregular columns, moderately regular columns (approximately regular columns), respectively.

Figure 11 displays the failure diagrams of the CJB samples with various regular degrees along the direction II perpendicular to the column axis under the lateral pressure of 6 MPa (the completely regular CJBs, the approximately regular CJBs, the moderately regular CJBs, the irregular CJBs). It can be seen from Figure 11(a)

that for completely regular CJBs, damage develops along the vertical and oblique joints. Near the joints, the damage develops, and the cracks initiate and propagate. In Figure 11(b), for the approximately regular CJBs, the vertical and oblique joints are damaged. In the upper area of the sample closing to the joints, the damage development and crack growth at the columns are obvious. As presented in Figure 11(c), for the moderately regular CJBs, some vertical joints get cracked, and other vertical and oblique joints are damaged. In the upper middle area of the sample, near the column corners, the extrusion effect is obvious, and there are damage development and crack growth. As shown in Figure 11(d), for the irregular CJBs, a few vertical joints get cracked and oblique joints are damaged. Near the middle of the specimen, due to the extrusion of the column corners and the compression-shear slip of the joints, the strip zones of damage develop and the crack initiation and propagation occur.

3.6. Effect of model boundaries on mechanical properties and AE energy of irregular CJBs under lateral pressure

Figure 12 shows the effect of boundary conditions on mechanical properties and AE energy of irregular CJBs. The case I corresponds to the case between plane stress and plane strain, and the case II corresponds to plane strain. From Figure 12(a), it can be seen that for the irregular CJBs along the direction I and the lateral pressure of 6 MPa, when the boundary condition is changed from the case I to the case II, the growth ratio of CS is 29.42%. For the irregular CJBs along the direction parallel to the column axis and $\beta = 30^\circ$, the increase ratio of CS is 8.30%. It can be seen that the increase is smaller. This is mainly because at $\beta = 30^\circ$, the CS of CJBs is obviously affected by the compression-shear slip of columnar joints. As depicted in Figure 12(b), for the irregular CJBs along the direction I and the lateral pressure of 6 MPa, when the boundary condition is changed from the case I to the case II, the growth ratio of EDM is 11.89%. For the irregular CJBs along the direction parallel to the column axis and $\beta = 30^\circ$, the increase ratio of EDM is 5.84%. Clearly, the increase is smaller. This is also because at $\beta = 30^\circ$, the influence of the compression-shear slip of columnar joints on EDM of CJBs is obvious.

Figure 12(c) shows the stress–strain relationship and AE energy of irregular CJBs along the direction I and with lateral pressure of 6 MPa, and with model boundary between the plane stress and the plane strain. From Figure 12(c), we can see that the AE energy indicates a less obvious distribution of double peaks. The first AE energy peak occurs before the stress peak and the second one is in the falling section after the stress peak. Figure 12(d) shows the stress–strain relationship and AE energy of the irregular CJBs along the direction parallel to the column axis when $\beta = 30^\circ$, and with the boundary condition between the plane stress and the plane strain. As depicted in Figure 12(d), the AE energy is distributed in a triple-peaks way. The first peak is near the stress peak, and the second and third peaks are in the falling section after the stress peak.

Figure 12(e) shows the effect of various model boundaries on the accumulated AE energy before the stress peak of CJBs. It is clear from Figure 12(e) that for the

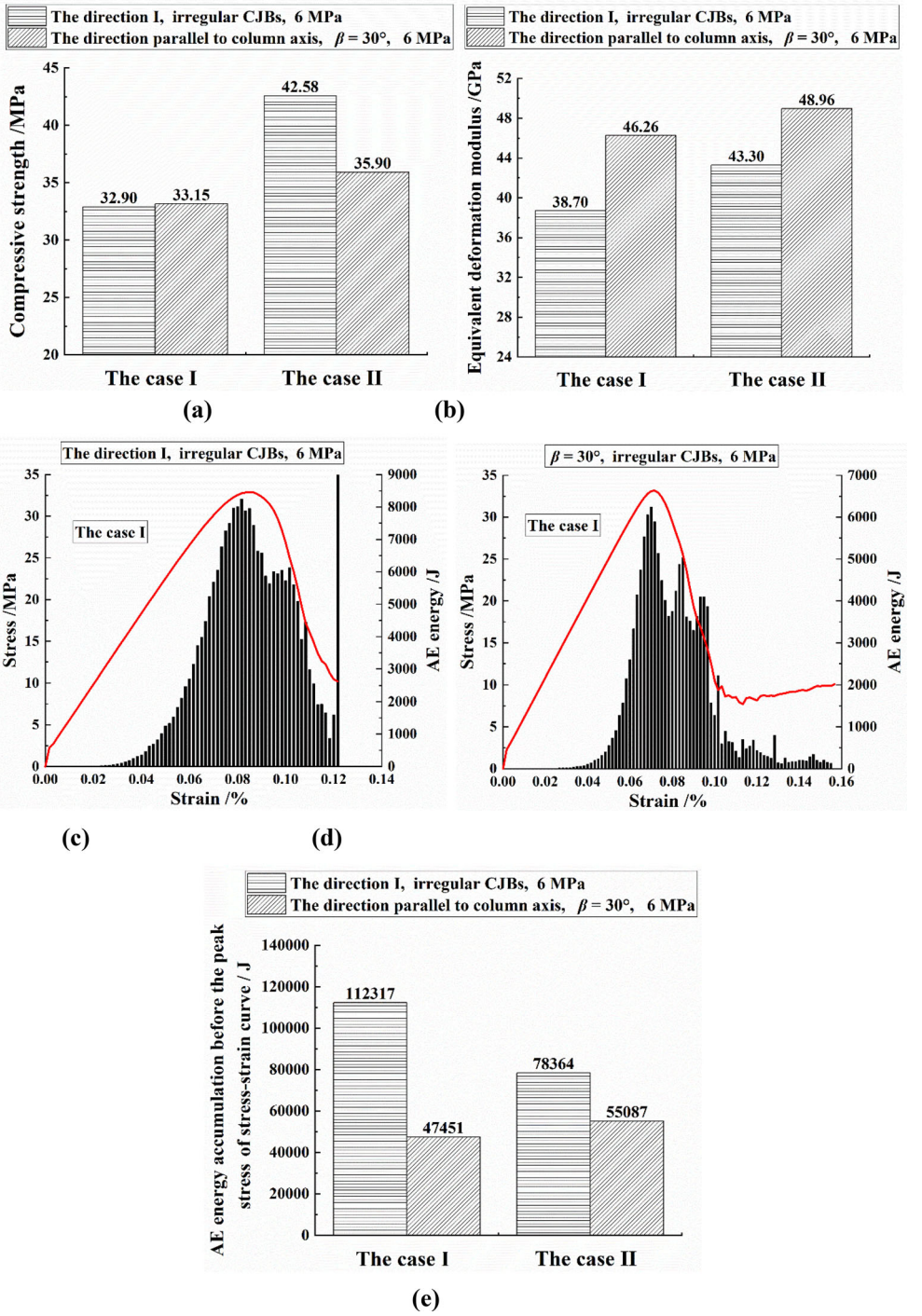

Figure 12. Effect of boundary condition on mechanical parameters and AE energy of CJBs: (a) compressive strengths; (b) equivalent deformation moduli; (c,d) stress–strain curves and AE energy; (e) accumulated AE energy before the stress peaks (the cases I and II correspond to the case between plane stress and plane strain, and the case of plane strain, respectively).

irregular CJBs along the direction I and with lateral pressure of 6 MPa, if the boundary condition is transformed from the case I to the case II, the accumulated AE energy before stress peak decreases from 112,317 to 78,364 J, with a decrease ratio of −30.23%. For the irregular CJBs along the direction parallel to the column axis and $\beta = 30^\circ$, the accumulated AE energy before stress peak grows from 47,451 to 55,087 J, with an increase ratio of 16.09%. It demonstrates that for an underground cavern, the energy released by rock mass at a certain depth inside the walls is likely to be higher than that released by rock mass near the walls. The monitoring and supporting measures should be conducted for the rock mass at a certain depth inside the underground cavern walls.

4. Discussion

4.1. Fracture mechanism of CJBs under lateral pressure

Taking the irregular CJBs parallel to the column axis as an example, when $\beta = 30^\circ$ and the lateral pressure is 6 MPa, the failure mechanism can be summarized as follows: with the load growing, high stress concentrations appear at the columnar joints inside the sample. There is a tendency of compression-shear damage at some local locations of the joints. When the load grows, the compression-shear damage slip appears at the joints in the upper area of the sample. At the top of the sample, high stress concentration is obvious and the crack initiation occurs. The cracks further initiate and develop at the top of the specimen, and the stresses are concentrated at the edges of a few columns within the upper part of the sample. With the load further increasing, at the edges of some columns and at the original stress concentration areas, the cracks initiate and propagate, and there are stress concentrations occurring at the tips of the cracks. Eventually, the breakage of the columns intensifies at the upper part of the specimen.

Zhou et al. (2018) applied PFC2D to investigate the mechanical properties of single jointed specimens and double jointed specimens, but only considered the effect of lateral pressure on the fracture mechanisms of single jointed specimens. Chen et al. (2020) argued that the stress-strain curves of granite samples with open precut cracks show the characteristics of stepped brittle drop under various lateral pressures. This is related to the layout of precut cracks. Fan et al. (2015) used PFC3D to study the physico-mechanical parameters of multi-non-persistent jointed specimens suffering uniaxial compression. They analysed the variation of compressive strength of specimens with the growth of joint dip angle and length. With the length of joints increasing, the compressive strength of specimens was more sensitive to the joint dip angle. However, the effect of lateral pressure on the fracture mechanisms of jointed rock masses was not fully considered in their research. Xue et al. (2021) investigated time-dependent/time-independent deformation and fracture of double-notched sandstone samples by DIC to reveal the related crack paths and failure modes of sandstone. Nevertheless, the energy evolutions during the fracturing processes of the samples remain unclear. Wu et al. (2019) numerically investigated the anisotropy of jointed rock mass under lateral pressure. However, in their study, the joint dip angle obeyed the normal distribution, the joint trace length obeyed the lognormal distribution, and

the joint space obeyed the negative exponential distribution or lognormal distribution. Therefore, the fracture mechanisms of their specimens depends on the related statistical distribution.

4.2. Effect of rock inhomogeneity on mechanical properties and AE energy of jointed rock mass under lateral pressure

Along the direction parallel to the column axis, when the inhomogeneity index is 5 or 10 and the lateral pressure is 2, 4, 6 or 8 MPa, there is a U-shaped trend of the CS of the sample with the dip angle of columns increasing. When the dip angle $\beta = 15°–60°$, the influence of the inhomogeneity index on the CS of specimen is very small. When the dip angle β is 0°, 75° or 90°, the influence of inhomogeneity index on that is obvious.

Under the lateral pressures of 2 and 6 MPa, along the direction parallel to the column axis, in terms of the sequence of the occurrence on the strain axis, the inhomogeneity indexes for accumulated AE energy corresponding to the strength peaks of specimens are 10 and 5, respectively; that is, for the direction parallel to the column axis and $\beta = 30°$, the less rock inhomogeneity, the more forward the accumulated AE energy corresponding to the stress peak on the strain axis. In the aspect of AE energy accumulation magnitude from little to large, the inhomogeneity indexes for that are 5 and 10, respectively, but the difference is small.

Liu et al. (2018) investigated the mechanical parameters of brittle rocks effected by micro-geometric inhomogeneity. The crack initiation stress, crack damage stress and strength peak were calculated numerically. However, the effect of the joint dip angle on physico-mechanical parameters and AE energy of rock mass was not fully considered. Sabri et al. (2016) analysed the effect of particle size heterogeneity on roughness of fracture surface and failure mechanisms of rocks. In their research, the influence of lateral pressure was not considered. Li et al. (2018) investigated the effect of inhomogeneity on deformation behaviours and AE release of stratified rock samples under uniaxial compression by the DIP-based finite difference method, but the influence of lateral pressure on AE energy was not further analysed. Jiao et al. (2005) found that with the heterogeneity of faults in geometry increasing, the AE corresponding to the stress peak lags in the loading stage. This phenomenon is similar with the results of this paper to a certain extent. Namely, the more inhomogeneous the rock is, the farther the accumulated AE energy corresponding to the stress peak of CJB in the loading stage lags. Li and Li (2010) discussed the effect of inhomogeneity on AE features of rock sample, but the influence of joint and lateral pressure were not considered further.

4.3. Effect of irregularity degree of columns on mechanical parameters and AE energy of jointed rock mass under lateral pressure

The square samples with various irregularity degrees of columns along the directions I and II perpendicular to the column axis were established. Then, a group of uniaxial compression tests were performed as shown in Figure 13. It can be seen

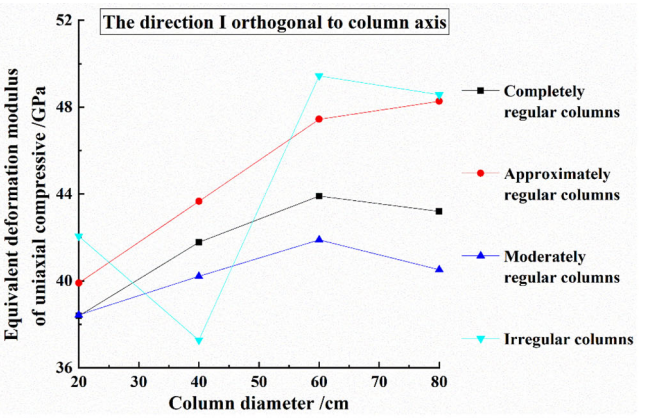

(a)

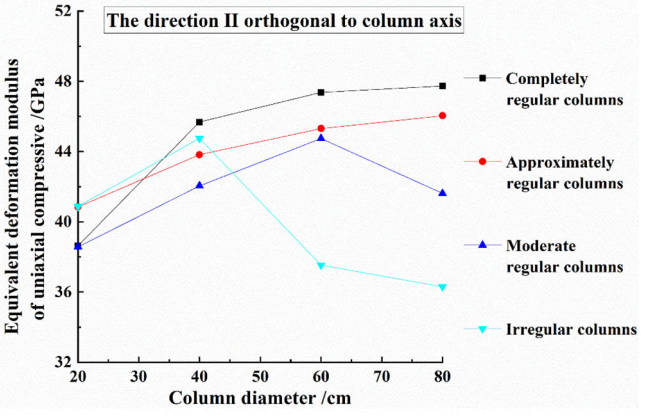

(b)

Figure 13. (a) Equivalent deformation modulus of samples with various irregularity degrees of columns along the direction I perpendicular to column axis; (b) along the direction II perpendicular to column axis.

that the changing range of EDM of CJBs containing irregular columns along the direction I perpendicular to the column axis is widest. Besides, when the column diameters are 20, 60 and 80 cm, the EDM of irregular columns in the direction I is the largest than the other regularity degrees of columns. This phenomenon agrees with the results by Cui et al. (2016) very well. Furthermore, for the square samples along the direction II perpendicular to the column axis, the EDMs of CJBs containing irregular columns are higher than the other relatively regular columns when the column diameters are 20 and 40 cm. From the perspective of mechanical mechanism, this is because under uniaxial compression, the occlusal degree between irregular columns is high, and the relative anti-sliding ability between joints get strengthened.

Then, Figure10 (a,c) show that, on the whole, along the direction I perpendicular to the column axis, when the lateral pressure is 6 MPa, the EDMs of specimens with approximately regular columns are the largest; along the direction II perpendicular to

the column axis, the EDMs of specimens with completely regular columns are the largest. From the perspective of mechanical mechanism, this is because the lateral pressure enhances the occlusal degree between columns and improves the anti-sliding ability of joints.

Kulatilake et al. (1993) pointed out that the deformation modulus and shear modulus of jointed rock masses gradually drop with the number of joints and the ratio of joint size to rock block size increasing, which is consistent with the results along the direction II in this paper. Namely, with the column irregularity increasing, the EDM of CJBs will decrease. Bhasin and Hoeg (1998) investigated the mechanical parameters of samples with three different block sizes under lateral pressure. The results showed that the specimens with smaller block size (smaller joint spacing) had larger compressive strength but smaller deformation modulus. Wang et al. (2020) used PFC to study the mechanical parameters of rock mass with two different joint densities. Their results demonstrates that the rock sample with high joint density had low uniaxial compressive strength and elastic modulus. These results agree with the obtained results along the directions I or II in this article. For example, the smaller the column diameter is, the lower the EDM of CJBs is.

5. Conclusion

With the aim of understanding the failure mechanism and energy release features of CJB affected by the lateral pressure, rock heterogeneity and column irregularity, the heterogeneous CJB models with various column dip angles, irregularity degrees of columns and boundary conditions were established using the DIC. Then, the gradual failure process and AE energy release of CJB were simulated under different lateral pressures. The influence factors of the mechanical behaviours of CJB were analysed. The main findings can be concluded as follows:

1. The rock heterogeneity shows the complex influence rule on mechanical properties and AE energy of CJBs. Clearly, the compressive strength of sample basically displays a U-shaped trend with the dip angle of columns increasing along the direction parallel to the column axis when the inhomogeneity index is 5 or 10. And the compressive strength affected by the inhomogeneity index also depends on the dip angle β. Furthermore, when the inhomogeneity index is 5 or 10 and the lateral pressure is 2, 4, 6 or 8 MPa, the EDM of specimen decreases in the beginning, then increases and then drops with the dip angle increasing. Besides, the EDM of sample is more sensitive to the inhomogeneity index than the lateral pressure.
2. The irregularity degree of columns has been proven to be a critical influence factor. Along the direction I perpendicular to the column axis, the compressive strength of sample initially increases and then decreases with the column irregularity degree increasing when the lateral pressure is 6 MPa. However, along the direction II perpendicular to the column axis, the compressive strength decreases with the irregularity degree of columns growing under the same lateral pressure. Along the direction I/II perpendicular to the column axis, in terms of the

occurrence sequence of accumulated AE energy corresponding to the strength peaks of specimens on the strain axis, the columns will be irregular columns, moderately regular columns, approximately regular columns, completely regular columns, respectively.

3. The mechanical properties and AE energy of irregular CJBs are greatly affected by the model boundaries. Along the direction I under the lateral pressure of 6 MPa, when the boundary condition is changed from the case I to the case II, the growth ratio of the compressive strength of the irregular CJBs is larger than along the direction parallel to the column axis with $\beta = 30^{\circ}$. Along the direction I under the lateral pressure of 6 MPa, when the boundary condition is transformed from the case I to the case II, the accumulated AE energy of the irregular CJBs before stress peak decreases. However, along the direction parallel to the column axis with $\beta = 30^{\circ}$, the accumulated AE energy of irregular CJBs before stress peak grows.

Disclosure statement

No potential conflict of interest was reported by the authors.

Funding

The study was funded by the National Natural Science Foundation of China (Grant No. 42102314) and the China Postdoctoral Science Foundation (Grant No. 2020M680950).

References

Bhasin R, Hoeg K. 1998. Numerical modelling of block size effects and influence of joint properties in multiply jointed rock (Reprinted from Tunnelling and Underground Space Technology, vol 12, 1997). Tunn Undergr Space Technol. 13(2):181–188.

Chao ZM, Ma GT, Hu XW, Luo G. 2020. Research on anisotropic permeability and porosity of columnar jointed rock masses during cyclic loading and unloading based on physical model experiments. Bull Eng Geol Environ. 79(10):5433–5454.

Chen GQ, Sun X, Wang JC, Wang D, Zhu ZF. 2020. Detection of cracking behaviors in granite with open precut cracks by acoustic emission frequency spectrum analysis. Arab J Geosci. 13(6):258.

Cui Z, Wei Q, Hou J, Sheng Q, Li LQ. 2016. Structural effect on equivalent modulus of deformation of columnar jointed rock mass with jointed finite element method. Rock Soil Mech. 37(10):2921–2928, 2936.

Fan X, Kulatilake P, Chen X. 2015. Mechanical behavior of rock-like jointed blocks with multi-non-persistent joints under uniaxial loading: A particle mechanics approach. Eng Geol. 190:17–32.

Feng XH, Gong B, Tang CA, Zhao T. 2022. Study on the non-linear deformation and failure characteristics of EPS concrete based on CT-scanned structure modelling and cloud computing. Eng Frac Mech. 261:108214.

Gong B, Liang Z, Liu X. 2022. Nonlinear deformation and failure characteristics of horseshoe-shaped tunnel under varying principal stress direction. Arab J Geosci. 15:475.

Gui Y, Zhao GF. 2015. Modelling of laboratory soil desiccation cracking using DLSM with a two-phase bond model. Comput Geotech. 69:578–587.

Haeri H, Sarfarazi V, Zhu ZM. 2018a. PFC3D simulation of the effect of particle size on the single edge-notched rectangle bar in bending test. Struct Eng Mech. 68:497–505.
Haeri H, Sarfarazi V, Zhu ZM, Hedayat A, Marji MF. 2018b. Investigation of the model scale and particle size effects on the point load index and tensile strength of concrete using particle flow code. Struct Eng Mech. 66:445–452.
Haeri H, Sarfarazi V, Zhu ZM, Marji MF. 2018c. The effect of particle size on the edge notched disk (END) using particle flow code in three dimension. Smart Struct Syst. 22: 663–673.
Haeri H, Sarfarazi V, Zhu ZM, Moradizadeh M. 2018d. The effect of ball size on the hollow center cracked disc (HCCD) in Brazilian test. Comput Concr. 22:373–381.
Ji H, Zhang JC, Xu WY, Wang RB, Wang HL, Yan L, Lin ZN. 2017. Experimental investigation of the anisotropic mechanical properties of a columnar jointed rock mass: observations from laboratory-based physical modelling. Rock Mech Rock Eng. 50(7):1919–1931.
Jiao MR, Tang CA, Sun WF, Wang SH. 2005. Numerical studies of the influence of heterogeneity on rock failure and induced earthquake precursors. Key Eng Mater. 297-300:2648–2653.
Jin CY, Li SG, Liu JP. 2018. Anisotropic mechanical behaviors of columnar jointed basalt under compression. Bull Eng Geol Environ. 77(1):317–330.
Ke ZQ, Wang HL, Xu WY, Lin ZN, Ji H. 2019. Experimental study of mechanical behaviour of artificial columnar jointed rock mass containing transverse joints. Rock Soil Mech. 40(02):660–667.
Kulatilake P, Wang S, Stephansson O. 1993. Effect of finite-size joints on the deformability of jointed rock in 3-dimensions. Int J Rock Mech Min Sci Geomech Abstr. 30(5):479–501.
Li A, Shao GJ, Su JB, Sun Y, Yu TT, Shi HG. 2018. Influence of heterogeneity on mechanical and acoustic emission behaviours of stratified rock specimens. Eur J Environ Civ Eng. 22(sup1):s381–s414.
Li LC, Tang CA, Zhu WC, Liang ZZ. 2009. Numerical analysis of slope stability based on the gravity increase method. Comput Geotech. 36(7):1246–1258.
Li LC, Yang TH, Liang ZZ, Zhu WC, Tang CA. 2011. Numerical investigation of groundwater outbursts near faults in underground coal mines. Int J Coal Geol. 85:276–288.
Li SC, Li GY. 2010. Effect of heterogeneity on mechanical and acoustic emission characteristics of rock specimen. J Cent South Univ Technol. 17(5):1119–1124.
Liang ZZ. 2005. Three-dimensional failure process analysis of rock and associated numerical tests [dissertation]. China: Northeastern University.
Liu G, Cai M, Huang M. 2018. Mechanical properties of brittle rock governed by micro-geometric heterogeneity. Comput Geotech. 104:358–372.
Liu HN, Wang JM, Wang SJ. 2010. Experimental research of columnar jointed basalt with true triaxial apparatus at Baihetan Hydropower Station. Rock Soil Mech. 31(S1):163–171.
Liu XZ, Tang CA, Li LC, Lv PF, Liu HY. 2017. Microseismic monitoring and 3D finite element analysis of the right bank slope, Dagangshan Hydropower Station, during reservoir impounding. Rock Mech Rock Eng. 50(7):1901–1917.
Mazars J, Pijaudier-Cabot G. 1989. Continuum damage theory–application to concrete. J Eng Mech. 115(2):345–365.
Ni HJ, Xu WY, Shi AC, Xu JR, Ji H. 2015. Scale effect on equivalent continuum elastic modulus of columnar jointed rock masses by distinct element method. Eng Mech. 32(03):90–96.
Phillips JC, Humphreys MCS, Daniels KA, Brown RJ, Witham F. 2013. The formation of columnar joints produced by cooling in basalt at Staffa, Scotland. Bull Volcanol. 75(6):715.
Que XC, Zhu ZD, Niu ZH, Lu WN. 2021. Estimating the strength and deformation of columnar jointed rock mass based on physical model test. Bull Eng Geol Environ. 80(2): 1557–1570.
Sabri M, Ghazvinian A, Nejati HR. 2016. Effect of particle size heterogeneity on fracture toughness and failure mechanism of rocks. Int J Rock Mech Min Sci. 81:79–85.
Shi AC, Wei YF, Zhang YH, Tang MF. 2020. Study on the strength characteristics of columnar jointed basalt with a true triaxial apparatus at the Baihetan Hydropower Station. Rock Mech Rock Eng. 53(11):4947–4965.

Sun PF, Yang TH, Yu QL, Shen W. 2012. Numerical research on anisotropy mechanical parameters of fractured rock mass. Adv Mater Res. 524–527:310–316.
Tang CA, Kou SQ. 1998. Crack propagation and coalescence in brittle materials under compression. Eng Fract Mech. 61(3-4):311–324.
Tang CA, Lin P, Wong RHC, Chau KT. 2001. Analysis of crack coalescence in rock-like materials containing three flaws - Part II: numerical approach. Int J Rock Mech Min Sci. 38(7): 925–939.
Tang CA, Tang SB, Gong B, Bai HM. 2015. Discontinuous deformation and displacement analysis: From continuous to discontinuous. Sci China Technol Sci. 58(9):1567–1574.
Wang X, Yuan W, Yan YT, Zhang X. 2020. Scale effect of mechanical properties of jointed rock mass: a numerical study based on particle flow code. Geomech Eng. 21:259–268.
Wang YY, Gong B, Tang CA, Zhao T. 2022. Numerical study on size effect and anisotropy of columnar jointed basalts under uniaxial compression. Bull Eng Geol Environ. 81(1):41.
Weinberger R, Burg A. 2019. Reappraising columnar joints in different rock types and settings. J Struct Geol. 125:185–194.
Wu N, Liang ZZ, Li YC, Li H, Li WR, Zhang ML. 2019. Stress-dependent anisotropy index of strength and deformability of jointed rock mass: insights from a numerical study. Bull Eng Geol Environ. 78(8):5905–5917.
Xia YJ, Zhang CQ, Zhou H, Hou J, Su GS, Gao Y, Liu N, Singh HK. 2020. Mechanical behavior of structurally reconstructed irregular columnar jointed rock mass using 3D printing. Eng Geol. 268:105509.
Xiao WM, Deng RG, Fu XM, Wang CY. 2014. Model experiments on deformation and strength anisotropy of columnar jointed rock masses under uniaxial compression. Chin J Rock Mech Eng. 33(05):957–963.
Xiao WM, Deng RG, Fu XM, Wang CY. 2015. Experimental study of deformation and strength properties of simulated columnar jointed rock masses under conventional triaxial compression. Chinese Journal of Rock Mechanics and Engineering. 34(S1):2817–2826.
Xu T, Fu M, Yang S-Q, Heap MJ, Zhou G-l. 2021. A numerical meso-scale elasto-plastic damage model for modeling the deformation and fracturing of sandstone under cyclic loading. Rock Mech Rock Eng. 54(9):4569–4591.
Xu T, Ranjith PG, Wasantha PLP, Zhao J, Tang CA, Zhu WC. 2013. Influence of the geometry of partially-spanning joints on mechanical properties of rock in uniaxial compression. Eng Geol. 167:134–147.
Xue YC, Xu T, Zhu WC, Heap MJ, Heng Z, Wang XW. 2021. Full-field quantification of time-dependent and -independent deformation and fracturing of double-notch flawed rock using digital image correlation. Geomech Geophys Geo-Energ Geo-Resour. 7:100.
Yan DX, Xu WY, Wang W, Shi C, Shi AC, Wu GY. 2012. Research of size effect on equivalent elastic modulus of columnar jointed rock mass. Chin J Geotech Eng. 34(02):243–250.
Yan L, Xu WY, Wang RB, Meng QX. 2018. Numerical simulation of the anisotropic properties of a columnar jointed rock mass under triaxial compression. EC. 35(4):1788–1804.
Yang TH, Wang PT, Xu T, Yu QL, Zhang PH, Shi WH, Hu GJ. 2015. Anisotropic characteristics of jointed rock mass: a case study at Shirengou iron ore mine in China. Tunn Undergr Space Technol. 48:129–139.
Yu QL, Yang TH, Tang SB, Liu HL, Liang ZZ, Zheng X, Jia P. 2015. The 3D reconstruction method for quasi-brittle material structure and application. Eng Mech. 32(11):51–62, 114.
Yu XY, Xu T, Heap MJ, Baud P, Reuschle T, Heng Z, Zhu WC, Wang XW. 2021. Time-dependent deformation and failure of granite based on the virtual crack incorporated numerical manifold method. Comput Geotech. 133:104070.
Yuan Y, Xu T, Heap MJ, Meredith PG, Yang TH, Zhou GL. 2021. A three-dimensional meso-scale model for progressive time-dependent deformation and fracturing of brittle rock with application to slope stability. Comput Geotech. 135:104160.
Zheng WT, Xu WY, Ning Y, Meng GT. 2010. Scale effect and anisotropy of deformation modulus of closely jointed basaltic mass. J Eng Geol. 18(04):559–565.

Zhou GL, Xu T, Heap MJ, Meredith PG, Mitchell TM, Sesnic ASY, Yuan Y. 2020. A three-dimensional numerical meso-approach to modeling time-independent deformation and fracturing of brittle rocks. Comput Geotech. 117:103274.

Zhou GL, Xu T, Konietzky H, Zhu WC, Heng Z, Yu XY, Zhao Y. 2022. An improved grain-based numerical manifold method to simulate deformation, damage and fracturing of rocks at the grain size level. Eng Anal Boundary Elem. 134:107–116.

Zhou JR, Wei J, Yang TH, Zhu WC, Li LC, Zhang PH. 2018. Damage analysis of rock mass coupling joints, water and microseismicity. Tunn Undergr Space Technol. 71:366–381.

Zhou JX, Zhou Y, Gao YT. 2018. Effect mechanism of fractures on the mechanics characteristics of jointed rock mass under compression. Arab J Sci Eng. 43(7):3659–3671.

Zhu DJ, Yang LD, Cai YC. 2009. Research on anisotropic characteristics and size effect of columnar jointed rock mass. Chin J Rock Mech Eng. 28(07):1405–1414.